Bulletin of the JSME Vol.14, No.1, 2019
Journal of Biomechanical Science and Engineering

Development of a coupled human fluid numerical model for the evaluation of tsunami drowning hazards

Daiki AJIMA*, Takashi NAKAMURA*, Tatsuto ARAKI*, Tetsunori INOUE** and Akane KURISU***
* Department of Transdisciplinary Science and Engineering, Tokyo Institute of Technology
4259, Nagatsuta-cho, Midori-ku, Yokohama, Kanagawa, 226-8503, Japan
E-mail: ajima.d.aa@m.titech.ac.jp
** Port and Airport Research Institute, National Institute of Maritime, Port and Aviation Technology
3-1-1, Nagase, Yokosuka, Kanagawa, 239-0826, Japan
*** Independent researcher
3-7-10, Akatsutsumi, Setagaya-ku, Tokyo, 156-0044, Japan

Received: 6 July 2018; Revised: 1 November 2018; Accepted: 26 November 2018

Abstract
A numerical simulation model for the evaluation of the effectiveness of lifejackets against drowning in tsunamis considering both unsteady water currents and human movement was developed. The Constrained Interpolation Profile-Combined Unified Procedure scheme was combined with the link segment model to simulate interactions between the fluid and subjects in the developed model. The developed model was experimentally validated using a large flume. A manikin laid on blocks was swept down by a tsunami-like water current and caught by a vortex behind the blocks. The developed model accurately reproduced both water currents and the movement of the manikin and was thus considered adequate to analyze the movement of human bodies in tsunamis. The model was then used to analyze the movement of a human body in the same currents but with higher buoyancy, assumed to represent a lifejacket. Consequently, buoyancy greater than a human's body weight was required to keep the subject afloat; a buoyancy corresponding to the body weight caused the total submergence of the entire subject. Through comparison of forces applied to the body with its movement, it is revealed that a human body receives strong downward force while and immediately after passing over the vortex. These forces are caused due to the attractive pressure at the center of the vortex and downward currents in the downstream side of the vortex. These forces are considered to be remarkable in the evaluation of lifejackets in actual tsunamis.

Keywords : Biofluid mechanics, Drowning, Tsunami, Lifejacket, Human body dynamics, CIP-CUP scheme, Link segment model, Multiphase flow analysis

1. Introduction

Tsunamis pose large drowning risks and often have high death tolls. Approximately 91% of the more than 15,000 deaths that occurred in the 2011 off the Pacific coast of Tohoku earthquake were caused due to drowning in the subsequent tsunamis (National Police Agency, 2012). Swift evacuation to elevations is the most important measure to prevent tsunami-related deaths. However, it can often be difficult to quickly execute these evacuations; the tsunami following the 2011 off the Pacific coast of Tohoku earthquake reached some cities within 30 minutes (Muhari et al., 2012). Those who cannot evacuate on time, e.g., injured or elderly people or small children, find it difficult to keep themselves afloat. Therefore, a secondary measure that does not rely on human motion is necessary to prevent these people from drowning in future tsunamis.

For this purpose, the use of lifejackets is attracting attention. A lifejacket is a personal flotation device that provides face-up, in-water support to the user, regardless of human motion (International Organization for Standardization, 2006a). It can be used by people caught in tsunamis. Unlike most drowning incidents, tsunami victims are exposed to violent three-dimensional currents. However, ISO-12402 (International Organization for Standardization, 2006b) and other lifejacket

Paper No.18-00321
J-STAGE Advance Publication date : 6 December, 2018
[DOI: 10.1299/jbse.18-00321]

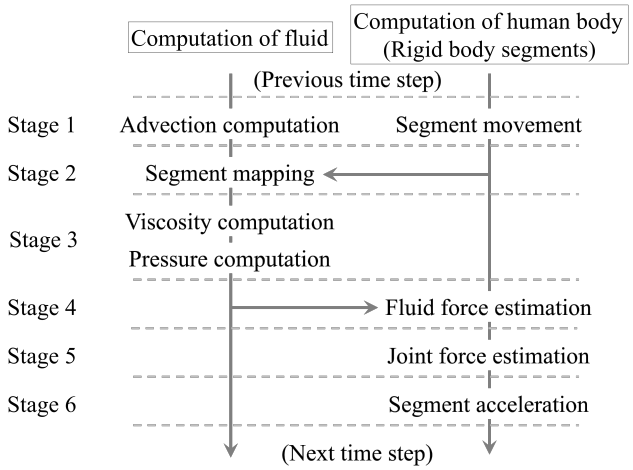

Fig. 1 Overview of the developed six-stage fluid and human motion computation procedure.

standards only require examinations in still water. Few researchers have examined the performance of lifejackets in tsunami-like currents. In one example, Kurisu et al. (2018) experimentally compared the movement of a manikin with and without a lifejacket in flows behind concrete blocks. As a fluid flows, backward-facing steps of the blocks can cause vertical vortexes to appear behind structures as they detach from the main flow. The research of Kurisu et al. (2018) showed that the manikin without wearing a lifejacket was rapidly drawn into water likely because of a vertical vortex, while the manikin wearing a lifejacket succeeded to keep afloat. This fact indicates not only potential of a lifejacket against tsunamis, but that violent water currents in tsunamis have higher hazards to drowning than still water. Thus performance evaluations of lifejackets not in still water but under tsunami-like currents such as vertical vortexes must be conducted to design and establish lifejackets as a valid measure against tsunamis.

Numerical analyses offer the possibility of these performance evaluation with the water currents. If once the numerical model would be developed, we could evaluate the efficacy of lifejackets under the various conditions such as the huge wave height that cannot be generated in an experimental flume. Existing numerical models representing the underwater movement of human bodies have mainly been developed from the standpoint of sports engineering. In one such model, Nakashima et al. (2007) developed a SWimming hUman Model (SWUM) to simulate the dynamics of a human body in various swimming motions. Mizuno and Yamakawa (2017) simulated the movement of a human body and the surrounding water flows in a dolphin kick motion. Some of these conventional models have evaluated the fluid force applied to a human body as the drag force derived from the relative velocity with still water or a steady flow. Additionally, periodic human movements were predefined to analyze and optimize specific swimming motions. However, in tsunamis, water runs unsteadily and subjects are forced into unsteady movement in and above the water. Therefore, a numerical model that supports direct fluid computation, represents unsteady movement of a human body, and examines the interactions between the two is essential.

A numerical model, i.e., the DRowning hUman Model (DRUM), was thus developed to represent the interactions of unsteady flow and human movement. A pilot study of DRUM was found in Nakamura et al. (2017). However, in this study, the model was applied only to human motion in a simple rectangular-shaped water container, wherein there is no dominant water flows. Therefore, while it was shown that the model can evaluate an accurate buoyancy force affecting to subjects, the model's performance for the tsunami wave was not considered at all. In this paper, first, the mathematical model used to describe fluid and human motion was discussed. Next, the developed model was evaluated by comparing experimental results from Kurisu et al. (2018) with the simulation results. Finally, the developed model was used to analyze human movement in tsunami-like currents with and without added buoyancy, which simulates the addition of a lifejacket.

2. Numerical simulation model

2.1. Basic concepts and fundamental equations

In this section, the basic concepts and fundamental equations used to develop the DRUM are explained. An overview of how the developed model computes and considers interactions between fluid and human motion is shown in Fig. 1.

[DOI: 10.1299/jbse.18-00321]

2.1.1. Fluid motion computation The Constrained Interpolation Profile-Combined Unified Procedure (CIP-CUP) scheme was used for computation of fluid motion (Yabe and Wang, 1991). To represent multiphase flow, the volume ratios of human body segments ϕ_s and air ϕ were introduced for each computational mesh, as shown in Fig. 2, where ϕ_s and ϕ represent the volume of a subject included in unit volume and that of air, respectively. By using ϕ_s and ϕ, the volume ratios of air, water, and body segments to a certain mesh can be represented as $(1-\phi_s)\phi$, $(1-\phi_s)(1-\phi)$, and ϕ_s, respectively. While the ϕ_s is updated by solving equation of motions of human body segments, the water surface is traced by the advection of ϕ with a CIP scheme (Yabe and Aoki, 1991; Yabe et al., 1991) without using any digitizer:

$$\frac{\mathrm{D}\phi}{\mathrm{D}t} = 0. \tag{1}$$

The flow velocity $\boldsymbol{u} = \left(u_x, u_y, u_z\right)$, pressure p, and density of air and water ρ_{air} and ρ_{water}, respectively, are solved with the common fundamental equations among all phases:

$$\frac{\mathrm{D}\boldsymbol{u}}{\mathrm{D}t} = -\frac{1}{\rho}\nabla p + \nabla\cdot(\nu\nabla)\boldsymbol{u} - \boldsymbol{g}, \tag{2}$$

$$\frac{\mathrm{D}p}{\mathrm{D}t} = -C^2\rho\left(\nabla\cdot\boldsymbol{u}\right), \text{ and} \tag{3}$$

$$\frac{\mathrm{D}\rho_l}{\mathrm{D}t} = -\rho_l\left(\nabla\cdot\boldsymbol{u}\right) \ \ (l = \text{air, water}). \tag{4}$$

These equations are applied to all meshes regardless of which material exists in the mesh. $\boldsymbol{g}$ is the gravitational acceleration, C is the speed of sound, ρ is the density, and $\nu = \nu_{\mathrm{mol}} + \nu_{\mathrm{SGS}}$ is composed of the molecular kinematic viscosity ν_{mol} and sub-grid-scale kinematic viscosity ν_{SGS}. In this work, it is assumed that conditions of human body segment's surface do not affect to the viscosity and that the ν_{SGS} is not influenced by interfaces between the air, water, and body segments. Under those assumption, the kinematic viscosity is determined from the weighted average of fluid based on the volume ratio ϕ: $\nu = \nu_{\mathrm{mol}} + \nu_{\mathrm{SGS}} = \phi\nu_{\mathrm{mol|air}} + (1-\phi)\nu_{\mathrm{mol|water}} + \nu_{\mathrm{SGS}}$. While $\nu_{\mathrm{mol|air}}$ and $\nu_{\mathrm{mol|water}}$ are molecular kinematic viscosity of air and water respectively, ν_{SGS} is determined by applying a standard expression to both area of air and water. The Smagorinsky coefficient is set to $C_s = 0.15$ (Kajishima, 2014). C and ρ are calculated as the weighted averages of air, water, and body segments based on the volume ratio: $C = (1-\phi_s)\phi C_{\mathrm{air}} + (1-\phi_s)(1-\phi)C_{\mathrm{water}} + \phi_s C_{\mathrm{solid}}$ and $\rho = (1-\phi_s)\phi\rho_{\mathrm{air}} + (1-\phi_s)(1-\phi)\rho_{\mathrm{water}} + \phi_s\rho_{\mathrm{solid}}$.

Each of these equations is divided into advection, viscosity, and pressure terms based on the fractional step method (Kim and Moin, 1985). Here, the advection terms are computed with a non-conservative CIP scheme (Yabe and Aoki, 1991; Yabe et al., 1991). While fluid mass is not strictly conserved by the scheme, as shown in subsection 3.3.1, the conservation error of total mass is assumed to be negligible in this work. Additionally, the surface tension of water surface is not computed in Eq. (2) because the flow solved in this work has large Weber number (see subsection 3.3.1).

2.1.2. Computation of human body segments The link segment model, which regards a human body as a collection of rigid segments connected at joints and has been used extensively in the literature, especially in sports engineering, was used to represent the human body (Fujii et al., 1995; Nakashima et al., 2007). A representative human (male) was selected from an anthropometric database (Kouchi and Mochimaru (2006); age: 23 years, height: 1.68 m, weight: 61.4 kg, and data ID: F020) and modeled with 5×10^{-3} m cubic voxels. This body was then divided into 10 segments ($s = 1, 2, \cdots, 10$) connected at nine joints ($j = 1, 2, \cdots, 9$) to compose a human-body model, as shown in Fig. 3.

The translation and rotation of the s-th segment connected to other segments(s) with the j-th joint(s) around the center of mass can then be represented by the Newton and Euler equations in Eq. (5) and Eq. (6), defined in the stationary axes and the s-th segment's principal axes of inertia, respectively.

$$\boldsymbol{M}_s\dot{\boldsymbol{v}}_s = \boldsymbol{F}_{s|\mathrm{fluid}} + \sum_{j\,\mathrm{on}\,s}\boldsymbol{F}_{s|j} - \boldsymbol{M}_s\boldsymbol{g} \ \text{ and} \tag{5}$$

$$\boldsymbol{I}_s\dot{\boldsymbol{\omega}}_s + \tilde{\boldsymbol{\omega}}_s\boldsymbol{I}_s\boldsymbol{\omega}_s = \boldsymbol{T}_{s|\mathrm{fluid}} + \sum_{j\,\mathrm{on}\,s}\left(\tilde{\boldsymbol{r}}_{sj}\boldsymbol{F}_{s|j} + \boldsymbol{T}_{s|j}\right), \tag{6}$$

where $\boldsymbol{M}_s$ and $\boldsymbol{I}_s$ are the s-th segment's mass and principal moment of inertia, respectively (see Fig. 4). $\boldsymbol{v}_s$ and $\boldsymbol{\omega}_s$ are the translation and angular velocity vector of the s-th segment, respectively. $\boldsymbol{F}_{s|\mathrm{fluid}}$ and $\boldsymbol{T}_{s|\mathrm{fluid}}$ are the force and torque, respectively, which the s-th segment receives from surrounding fluid. $\boldsymbol{F}_{s|j}$ and $\boldsymbol{T}_{s|j}$ are the force and torque, respectively, which s-th segment receives from the j-th joint. $\boldsymbol{r}_{sj}$ is the displacement from the s-th segment's center of mass to the j-th joint. and $\sum_{j\,\mathrm{on}\,s}$ represents the summation of all joints at which the s-th segment is connected with other segments. The operators $\dot{\boldsymbol{a}}$ and $\tilde{\boldsymbol{a}}\boldsymbol{b}$ denote the time derivative and vector product $\dot{\boldsymbol{a}} = \mathrm{d}\boldsymbol{a}/\mathrm{d}t$ and $\tilde{\boldsymbol{a}}\boldsymbol{b} = \boldsymbol{a}\times\boldsymbol{b}$, respectively.

[DOI: 10.1299/jbse.18-00321]

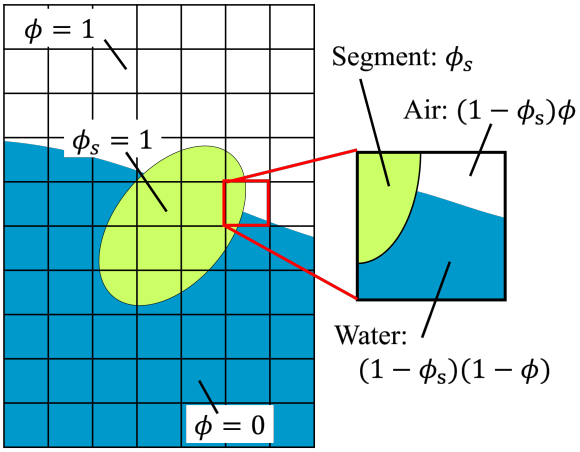

Fig. 2 Representation of multiphase fluid with the volume ratio of human body segments ϕ_s and air ϕ to the computational mesh.

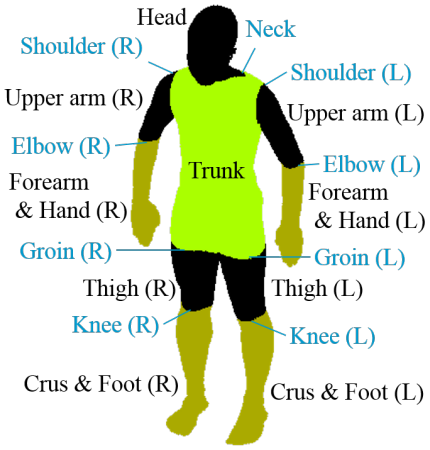

Fig. 3 Simulated human body segments (black letter) and joints (blue letter).

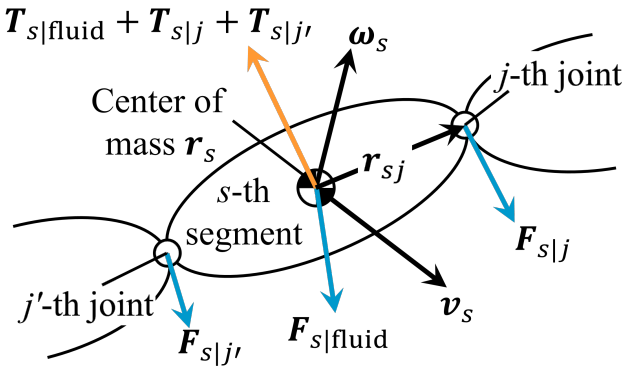

Fig. 4 Force and torque on a human body segment.

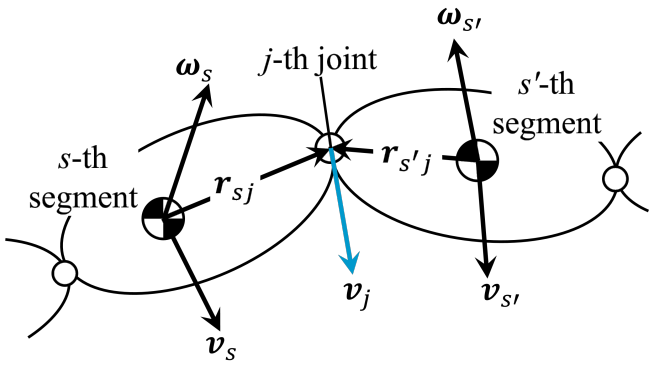

Fig. 5 A joint connecting a pair of human body segments.

2.2. Computational procedure

In this section, the procedure of each of the six computational stages is discussed (see Fig. 1).

Stage 1: Advection computation and segment movement The advection terms of Eqs. (1)–(4), i.e., $\mathrm{D}f/\mathrm{D}t = 0$ ($f = \phi, \boldsymbol{u}, p, \rho_l$), are solved for each mesh. The values of ϕ are calculated; the water surface of the next step is then traced. At the same time, the location of each human body segment is renewed based on its translational and rotational velocity determined in the previous time step.

Stage 2: Segment mapping In this stage, the location of each body segment is determined and its volume fraction ϕ_s is renewed for each mesh. The flow velocity of each mesh is then modified according to ϕ_s. When a computational mesh contains the s-th segment, its velocity at the center of this mesh is derived as

$$\boldsymbol{u}_s = \boldsymbol{v}_s + \tilde{\omega}_s \boldsymbol{r}_{s\mathrm{P}}, \tag{7}$$

where $\boldsymbol{r}_{s\mathrm{P}}$ is the displacement from s-th segment's center of mass to the center of the mesh. The flow velocity of the mesh is then modified using $\boldsymbol{u}_s$ as follows:

$$\boldsymbol{u}^{**} = \left(1 - \sum_{s\,\text{in mesh}} \phi_s\right)\boldsymbol{u}^* + \sum_{s\,\text{in mesh}} \phi_s \boldsymbol{u}_s, \tag{8}$$

where $\boldsymbol{u}^{**}$ is the modified flow velocity, $\boldsymbol{u}^*$ is the flow velocity derived in stage 1, and $\Sigma_{s\,\text{in mesh}}$ represents the summation of all body segments contained in the mesh. The use of Eq. (8) to modify the flow velocity corresponds to the application of the no-slip condition to the boundary between the fluid and human subject (Xiao, 1999).

Stage 3: Viscosity and pressure computation The viscosity term of Eq. (2), i.e., $\partial \boldsymbol{u}/\partial t = \nabla \cdot (\nu \nabla)\boldsymbol{u} - \boldsymbol{g}$, and the pressure terms of Eqs. (2)–(4), i.e., $\partial \boldsymbol{u}/\partial t = -\nabla p/\rho$, $\partial p/\partial t = C^2(\partial \rho/\partial t)$, and $\partial \rho_l/\partial t = -\rho_l \nabla \cdot \boldsymbol{u}$, respectively, are solved

[DOI: 10.1299/jbse.18-00321]

consecutively. In order to realize spatially continuous change of pressure, Eq. (3) is applied to all the meshes regardless of the volume ratio ϕ_s and ϕ. Gravity acceleration is also solved in this stage. The pressure of the next step p^{n+1} is calculated first through an iterative solution of the following Poisson's equation:

$$\nabla \cdot \left(\frac{\nabla p^{n+1}}{\rho^*} \right) - \frac{p^{n+1} - p^*}{\rho^* C^2 \Delta t^2} = \frac{\nabla \cdot \boldsymbol{u}}{\Delta t}, \tag{9}$$

where ρ^* and p^* represent the density and pressure calculated in stage 1, respectively. The flow velocity and density of the next step can then be sequentially calculated by accelerating with the calculated pressure.

Stage 4: Fluid force estimation In this stage, the force $\boldsymbol{F}_{s|\mathrm{fluid}}$ and torque $\boldsymbol{T}_{s|\mathrm{fluid}}$ from the fluid are estimated for each body segment by integrating the pressure ∇p and frictional stress $\boldsymbol{\tau}$ as

$$\boldsymbol{F}_{s|\mathrm{fluid}} = \sum_{\mathrm{meshes}} (\nabla p + \boldsymbol{\tau}) \phi_s \Delta V \quad \text{and} \tag{10}$$

$$\boldsymbol{T}_{s|\mathrm{fluid}} = \sum_{\mathrm{meshes}} (\tilde{\boldsymbol{r}}_{s\mathrm{P}} (\nabla p + \boldsymbol{\tau})) \phi_s \Delta V, \tag{11}$$

respectively, where Σ_{meshes} represents the summation of all meshes containing the s-th segment, $\boldsymbol{\tau} = \rho \nu \nabla \boldsymbol{u}$, and $\Delta V = \Delta x \Delta y \Delta z$ is the volume of each mesh.

Stage 5: Joint force estimation In this stage, the values of $\boldsymbol{F}_{s|j}$ and $\boldsymbol{T}_{s|j}$ are determined by assuming two main physical constraints for a human body. The joints are constrained such that (i) each specific body segment must remain in contact with given other segments and (ii) the joint angles between body segments remain within a movable extent. Therefore, according to the first constraint, when the s-th and s'-th segments are connected at the j-th joint (Fig. 5), the velocity of the j-th joint $\boldsymbol{v}_j$ must match with those of both segments (Fujii et al., 1995).

$$\boldsymbol{v}_j = \boldsymbol{v}_s + \tilde{\boldsymbol{\omega}}_s \boldsymbol{r}_{sj} = \boldsymbol{v}_{s'} + \tilde{\boldsymbol{\omega}}_{s'} \boldsymbol{r}_{s'j} \tag{12}$$

By substituting Eqs. (5) and (6) into the temporal derivative of Eq. (12), a conditional equation to be satisfied is derived as follows:

$$\begin{aligned} &(\boldsymbol{M}_s)^{-1} \left(\boldsymbol{F}_{s|\mathrm{fluid}} + \sum_{j \text{ on } s} \boldsymbol{F}_{s|j} \right) + \boldsymbol{t}_s \left(\boldsymbol{T}_{s|\mathrm{fluid}} + \boldsymbol{t}_s \boldsymbol{I}_s \sum_{j \text{ on } s} \boldsymbol{F}_{s|j} - \tilde{\boldsymbol{\omega}}_s \boldsymbol{I}_s \boldsymbol{\omega}_s \right) + \tilde{\boldsymbol{\omega}}_s \tilde{\boldsymbol{\omega}}_s \boldsymbol{r}_{sj} \\ &= (\boldsymbol{M}_{s'})^{-1} \left(\boldsymbol{F}_{s'|\mathrm{fluid}} + \sum_{j \text{ on } s'} \boldsymbol{F}_{s'|j} \right) + \boldsymbol{t}_{s'} \left(\boldsymbol{T}_{s'|\mathrm{fluid}} + \boldsymbol{t}_{s'} \boldsymbol{I}_{s'} \sum_{j \text{ on } s'} \boldsymbol{F}_{s'|j} - \tilde{\boldsymbol{\omega}}_{s'} \boldsymbol{I}_{s'} \boldsymbol{\omega}_{s'} \right) + \tilde{\boldsymbol{\omega}}_{s'} \tilde{\boldsymbol{\omega}}_{s'} \boldsymbol{r}_{s'j}, \end{aligned} \tag{13}$$

where $\boldsymbol{t}_s = -\tilde{\boldsymbol{r}}_{sj} \boldsymbol{A}_{\mathrm{O}s} (\boldsymbol{I}_s)^{-1}$ and $\boldsymbol{A}_{\mathrm{O}s}$ is a coordinate transformation matrix from the principal axes of the s-th segment to the stationary axes.

At each joint, the two connected body segments have orthonormal bases with rotational angles $\boldsymbol{\theta}_j = \left(\theta_{j1}, \theta_{j2}, \theta_{j3} \right)$, where each component of $\boldsymbol{\theta}_j$ is independent of the others. The maximum rotational angle for each component of each joint θ_{jl} ($l = 1, 2,$ and 3) was separately set based on Nakamura et al. (2016). To avoid reliance on the active motion of users and instead study only the impact of lifejacket usage in tsunami-like currents, no active drive of joints was considered herein. Passive resistance was modeled according to procedure followed in a previous research (Aoki and Yamazaki, 1998); negligible resistance is applied to joints within their movable extent until an exponential surge of resistance near the end of the extent. Therefore, no resistance is applied from the j-th joint as long as all components of $\boldsymbol{\theta}_j$ are inside their movable extents. The torque from the j-th joint $\boldsymbol{T}_{s|j}$ is regarded to be zero for any segment. Consequently, $\boldsymbol{F}_{s|j}$ can be derived from Eq. (13) alone. On the other hand, when a component of j-th joint's angle θ_{jl} reaches the full extent of its rotation, in order to satisfy the above constrain (b), a restoration force is applied based on the Voigt model:

$$\ddot{\theta}_{jl} = -c \dot{\theta}_{jl} + k \left(\theta_{jl} - \theta_{jl|\mathrm{limit}} \right), \tag{14}$$

where $\theta_{jl} - \theta_{jl|\mathrm{limit}}$ is the angle by which θ_{jl} exceeds the maximum or minimum value of its movable extent $\theta_{jl|\mathrm{limit}}$. The coefficients c and k are fixed, i.e., $c = 1/\Delta t$ and $k = c^2/4$, so that the joint angle shall be restored with a critical dumping. $\ddot{\boldsymbol{\theta}}_j$ in Eq. (14) is transformed to $\dot{\boldsymbol{\omega}}_j$ with the relationship:

$$\ddot{\boldsymbol{\theta}}_j = \dot{\boldsymbol{R}}_j \boldsymbol{\omega}_j + \boldsymbol{R}_j \dot{\boldsymbol{\omega}}_j, \tag{15}$$

where $\boldsymbol{R}_j$ is a transformation matrix between $\boldsymbol{\omega}_j$ and a temporal derivative of $\boldsymbol{\theta}_j$: $\boldsymbol{R}_j \boldsymbol{\omega}_j = \dot{\boldsymbol{\theta}}_j$ (Japan Society of Mechanical Engineer, 2006). By substituting both Eq. (4) and Eq. (15) for Eq. (14), Eq. (14) can be written as a conditional equation including $\boldsymbol{F}_{s|j}$ and $\boldsymbol{T}_{s|j}$. When the θ_{jl} reaches the full extent of its rotation, Eqs. (13) and (14) must be solved simultaneously to estimate $\boldsymbol{F}_{s|j}$ and $\boldsymbol{T}_{s|j}$.

[DOI: 10.1299/jbse.18-00321]

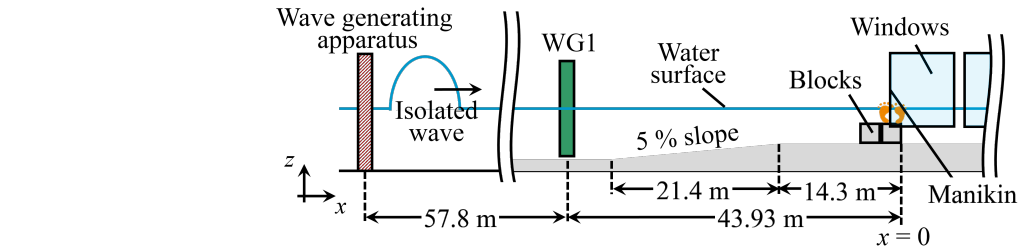

(a) Side view of the entire flume

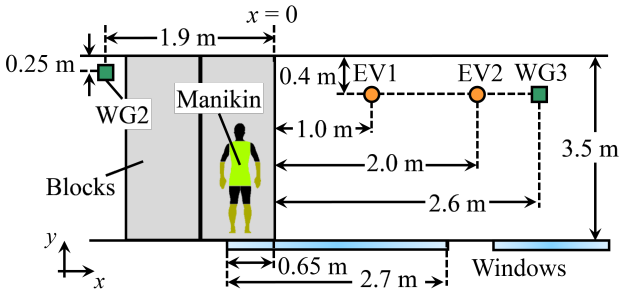

(b) Top view around the manikin

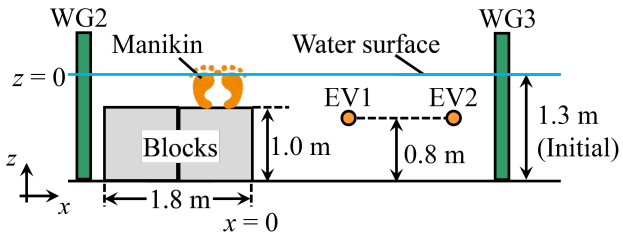

(c) Side view around the manikin

Fig. 6 Experimental flume, including the locations of water gauges (WG1, WG2, and WG3) and electromagnetic velocity meters (EV1 and EV2).

Stage 6: Segment acceleration The translational and rotational velocity of each body segment $\boldsymbol{v}_s$ and $\boldsymbol{\omega}_s$ of the next time step (Δt later) are calculated from the temporal integrations of Eqs. (5) and (6) using the Euler method.

3. Model validation through simulations of a human body in currents behind structures

3.1. Experimental design

In this section, to validate the model, we reproduced an experiment by Kurisu et al. (2018) wherein a manikin without a lifejacket was observed in tsunami-like water currents. The experimental flume used was a Large Hydro-Geo Flume (LHGF) at the Port and Airport Research Institute, Yokosuka Japan, as shown in Fig. 6. In each trial, a generated isolated wave traveled from the wave-generating apparatus settled in the upstream end of the flume. Upon reaching the blocks, the flow detached from the blocks, generating a vortex behind them in the downstream area.

Meanwhile, a manikin [Simulaids® Water Rescue Manikin; item number 1328; height: 164.5 cm and weight: 2.2 kgf (21.6 N) in water] was laid face up on the concrete blocks in the downstream area. The manikin closely resembled the human model used in the proposed simulation. The movement of the manikin was filmed for the duration of each trial through windows settled on the side wall of the flume. The relative location of the head was traced via an installed light-emitting diode. Additionally, the temporal variation of the water level in the chamber was measured using water gauges WG1, WG2, and WG3 (KENEK, CHT5-750BNC), as shown in Fig. 6. The temporal variation of the velocity in the x-direction and z-direction was measured with electromagnetic velocity meters EV1 and EV2 (KENEK, VM-801HFS).

3.2. Simulation conditions

The LHGF was then reproduced in the computational domain to validate the model. The computational domain is set to a section from 100 m on the upstream side to 30 m on the downstream side from the downstream-side edge of blocks: -100 m $\leq x \leq$ 30 m, where the origin of coordinate in mainstream direction x = 0 m corresponds to the downstream-side edge of blocks. A non-uniform orthogonal mesh was employed, where the x-direction, y-direction, and z-direction represent the mainstream, transverse, and vertical directions, respectively. In the space where the human moves (-1 m $\leq x \leq$ 6 m), the x-directional mesh (Δx) was uniformly 3 cm. The mesh size then increased with a constant ratio to Δx of 3.7 m at the furthest point upstream. The mesh size in the y-direction and z-direction (Δy and Δz, respectively) was 3 cm over the entire domain.

As an initial condition, instead of simulating strokes of the wave-generating apparatus, an incident sine wave was reproduced. From the experimental water-level variation observed at WG1, the wave height and wavelength of this wave

[DOI: 10.1299/jbse.18-00321]

were determined to be 0.44 and 48.2 m, respectively. This wave height is larger than the threshold value (0.2 m) that Japan Meteorological Agency (2013) would issue a tsunami advisory. Japan Meteorological Agency (2013) is appealing for the danger that people in seawater will get trapped due to the swift currents of tsunamis, even when the height is within the tsunami advisory range. Therefore, a consideration of the wave must be valuable, although the wave height (0.2 m) is smaller than that of historical huge tsunamis such as the tsunami of the 2011 Tohoku earthquake.

The simulated subject was located above the blocks with a similar initial position as the manikin. The velocity of each body segment was fixed at zero until reached by the wave at $t = 10$ s. A free boundary was applied to the x-directional edge of the computational domain. A no-slip wall was applied to the y-directional edge of the domain and the floor of the flume. The density of each segment was calculated to maintain the same weight with the manikin in water and to represent the situation of the experiment where both hands of the manikin were afloat in still water: 9.50×10^2 kg/m^3 for both forearms and hands, 9.98×10^2 kg/m^3 for both upper arms, and 1.04×10^3 kg/m^3 for the others. The movable extent of each joint was fundamentally set to the same value that was used in Nakamura et al. (2016), while components of the neck, shoulders, elbows, and knees were narrower and those of the groins are wider than the reference to fit the manikin.

The density and molecular kinematic viscosity of air and water were assumed to be the standard values at 20 °C: $\rho_{\mathrm{air}} = 1.30\,\mathrm{kg/m^3}$, $\rho_{\mathrm{water}} = 9.98 \times 10^2\,\mathrm{kg/m^3}$, $\nu_{\mathrm{mol|air}} = 1.49 \times 10^{-5}\,\mathrm{m^2/s}$, and $\nu_{\mathrm{mol|water}} = 1.01 \times 10^{-6}\,\mathrm{m^2/s}$. The bulk modulus of an acrylic resin $K = 7.5 \times 10^9$ Pa was adopted to represent the rigidity of segments. The computations were continued until $t = 25$ s, at which point the isolated wave reaches the downstream-end of the computational domain. The temporal increments of each computational step Δt were determined so that the CFL number and the change of joint angles within Δt remained less than or equal to 0.5 and 0.1 rad, respectively.

3.3. Simulation results

3.3.1. Fluid motion Figure 7 shows the variation of the water level observed at WG2 and WG3 [(a) and (b)] and the variation in the flow velocity in the x-direction and z-direction observed at EV1 [(c) and (d)] and EV2 [(e) and (f)]. The solid gray lines show the average of the 13 experimental trials; the dashed gray lines present the ranges of $\pm 3\sigma$, where σ is the sample standard deviation. These 13 experimental trials has the same condition of wave-generating apparatus, however they include the cases with different conditions of lifejacket buoyancy ranging from 0 kgf to 7 kgf. Similarly, the solid orange lines and dashed orange lines show the average and the ranges of $\pm 3\sigma$ of simulations which have different conditions of lifejacket in accordance with the experiments. Some cross-sectional snapshots of the water surface and flows from the side and top views are also shown in Figs. 8 and 9 .

In each simulation, the isolated wave with a height of approximately 0.65 m first reached the blocks ($t = 11$ s). The wave then passed over and detached from the blocks, forming a vortex behind them ($t = 12$ s). The wave broke at approximately $x = 1.5$ m ($t = 13$ s). The vortex then spread and weakened ($t \geq 14$ s). As shown in Figs. 7(b) and 8, the water level was maintained in the tsunami advisory range of Japan Meteorological Agency (2013) ($H \geq 0.2$ m) until $t \simeq 15$ s in any experimental trials and simulations. Furthermore, the simulated and experimental water flow velocity were in agreement until this time. Even after $t = 15$ s, as shown in Fig. (7), although the range of $\pm 3\sigma$ was considerable in both experimental and simulated velocity, the difference of the average and range of $\pm 3\sigma$ between experiment and simulation was still kept to be little. This considerable increasing of σ is likely due to the generation of localized and complex flows caused by specific reasons, e.g., wave breaking, steel pipes settling water gauges and velocity meters, an opening between the blocks, and manikin movement when it get closer to the wave gauges and velocity meters.

The relative error in conservation in total water volume was less than 0.37% until the end of simulation. An average change of water level caused by the conservation error is estimated to be no more than 1 cm. Thus the influence of using non-conservative CIP scheme is considered to be negligible. In Eq. (2), the surface tension is not taken into account. Observed flow speed of water is about $U = 1$ m/s (see Fig. 7). When the flow speed and the minimum scale size of human body segments (diameter of wrist $L = 5$ cm) are employed as typical scale, the Weber number can reach to several hundreds at least ($We = \rho_{\mathrm{water}} L U^2/\sigma = 6.8 \times 10^2$ where the surface tension of water $\sigma = 7.3 \times 10^{-2}$ N/m). Therefore, it is expected that the surface tension has no large influence on interactions between the body segment and water surface. Furthermore, even the surface tension is disregarded in the solution, as shown in Fig. 10, the calculated result can reproduce well a shape of water surface including a hydraulic jump observed around $t \simeq 12.5$ s.

3.3.2. Human-body movement Next, let us consider a temporal change of posture and movement of human-body being based on Figs. 8 and 9. In Fig. 8(a), the flow vectors and distribution of vorticity are shown on the cross section $y = 0$ m and the dashed squares represent the scope of Fig. 8(b). Similarly, the flow vectors and distribution of z-directional velocity are shown on the cross section $z = -0.5$ m in Fig. 9(a). Immediately after the wave reached the blocks, the human

[DOI: 10.1299/jbse.18-00321]

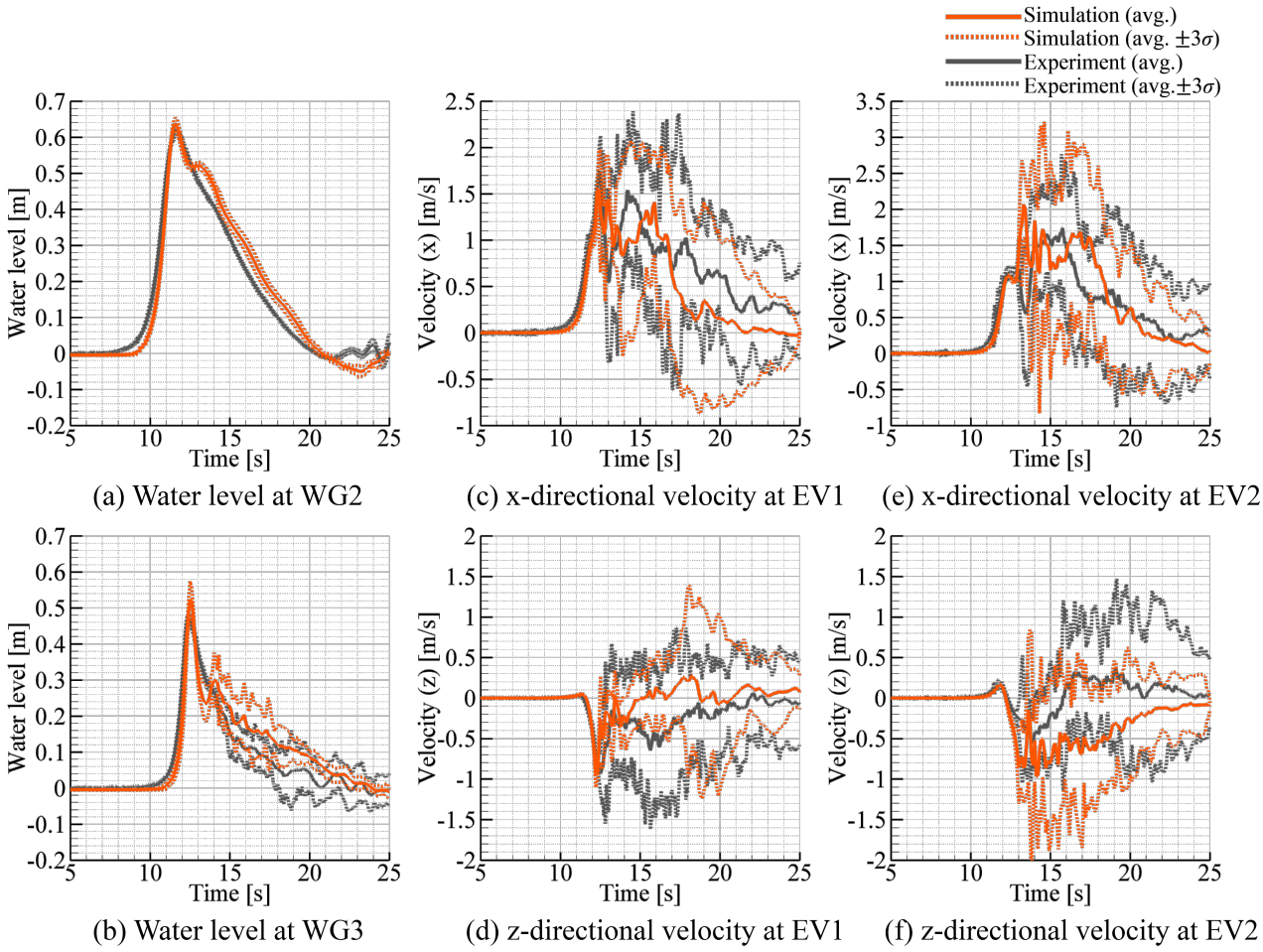

Fig. 7 (a,b) Water level, (c,e) x-directional velocity, and (d,f) z-directional velocity observed at the water gauges and the electromagnetic velocity meters in Fig. 6.

body was swept down from the blocks (t = 11–12 s). At this time, the entire body turned face-down (t = 12 s) because water currents pushed up its back. As the upper part of the body was pushed near the floor (t = 13–14 s), the legs were raised to the top of the blocks (z = -0.3 m) along with an edge of the vortex (t = 14 s). The legs were then swept away by the detached flow while the upper body and arms were raised (t = 17 s in the simulation; t = 14 s in the experiment). Finally, the head and the upper body were swept away to approximately x = 2.0 m (t = 19 s in the simulation; t = 15 s in the experiment).

In each of these scenes, the developed model accurately reproduced the postures and locations of the manikin, although the calculated speed of the body was found to have reduced after the body reached the bottom. This can also be seen in the head track comparison shown in Fig. 11, where the lines showing experimental and simulated tracks were in agreement, although the dots showing the location of every second were not in agreement after t = 13 s. Here, the experimental track below approximately z = -1.0 m (the arrow with a dotted line in Fig. 11) is not available because manikin was out of the scope where we could observe through the windows. The difference in the speed of the human body is caused because some body segments reached the floor (t = 14–15 s in Fig. 8(a)) and slowed down by the processes to apply the no-slip boundary condition. Naturally, CIP-CUP scheme can calculate repulsion between the colliding solid bodies. By solving Eq. (9) over a whole area including the human body, increasing of pressure and generation of repulsive force can be calculated in the collision between the human body and the floor. However, for the precise solution of the repulsion, the time increment Δt must be quite small in order to calculate a rapid propagation of elastic waves. In this work, to finish the simulation with an affordable elapsed time, a relatively larger Δt was employed. As a result, the human body was allowed to enter into the floor and slowed. Nevertheless, it is considered to be not important at all in evaluation of lifejackets. When evaluating lifejackets, the emphasis must be placed on verifying whether they can keep a human body afloat; thus, the movement of human bodies in areas around the floor are almost irrelevant to the evaluation.

[DOI: 10.1299/jbse.18-00321]

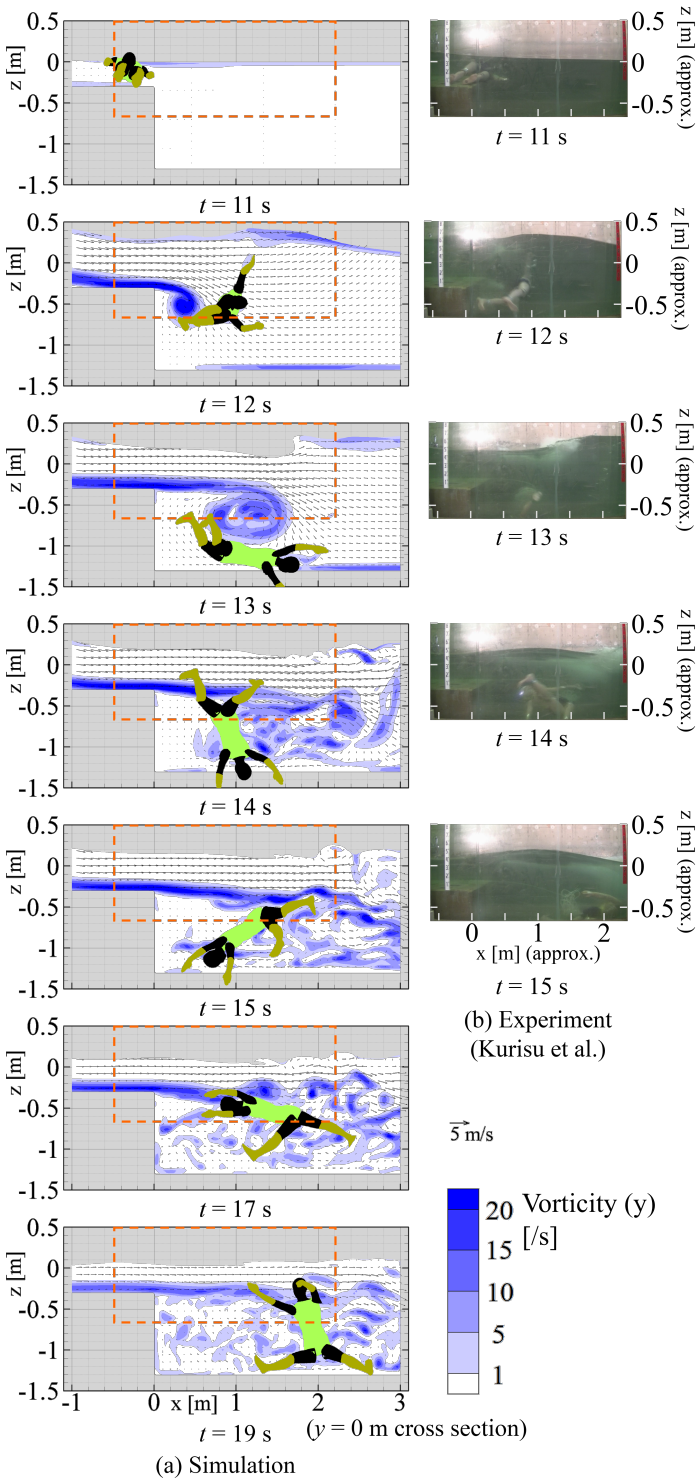

Fig. 8 Side-view snapshots of (a) simulated and (b) experimental flow interacting with a human body, where the dotted squares in (a) are the scope of (b).

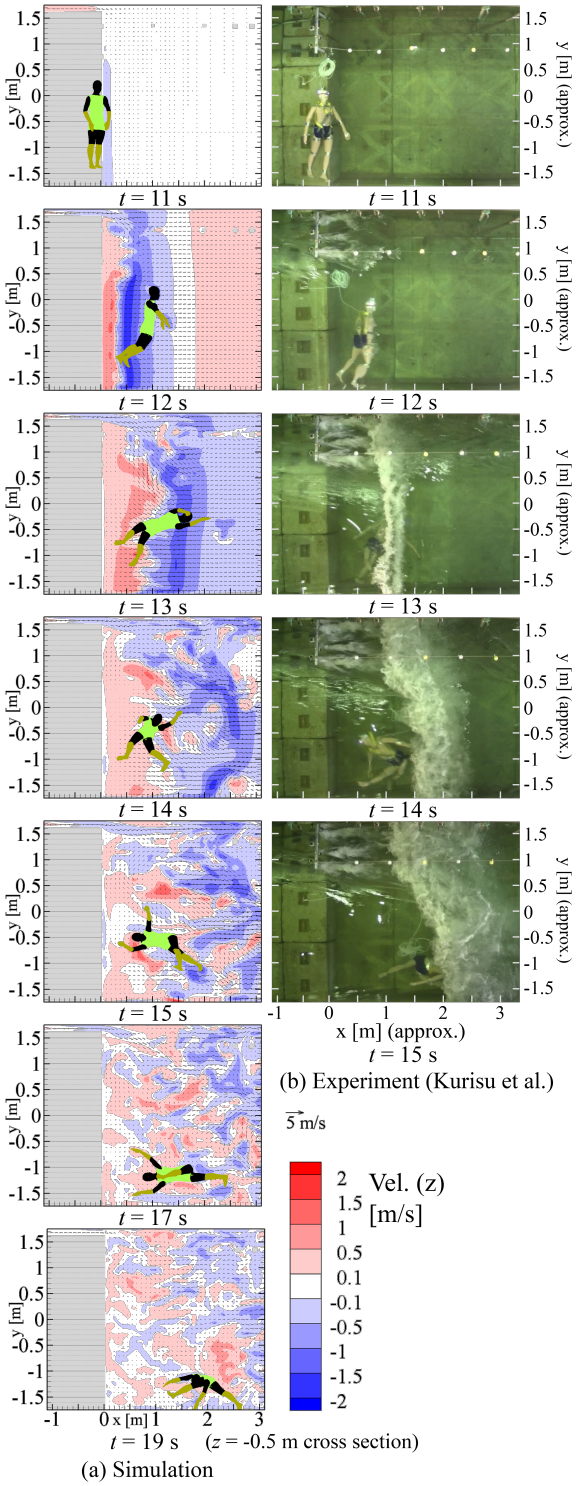

Fig. 9 Top-view snapshots of a **(a)** simulated and **(b)** experimental flow interacting with a human body.

Overall, the developed model accurately reproduced the shape of the water surface. The simulated water current profiles were generally within the range of the experimental error. Furthermore, the location and posture of the subject were well reproduced. The proposed model is therefore considered adequate to evaluate the movement of human bodies and the performance of lifejackets in tsunami-like water currents.

[DOI: 10.1299/jbse.18-00321]

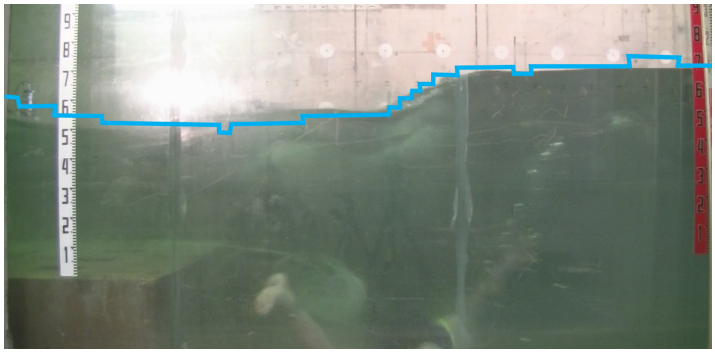

Fig. 10 Experimental shape of the water surface at t = 12.5 s. The blue line shows that of a simulation result at the same time on the y = 0 m cross section.

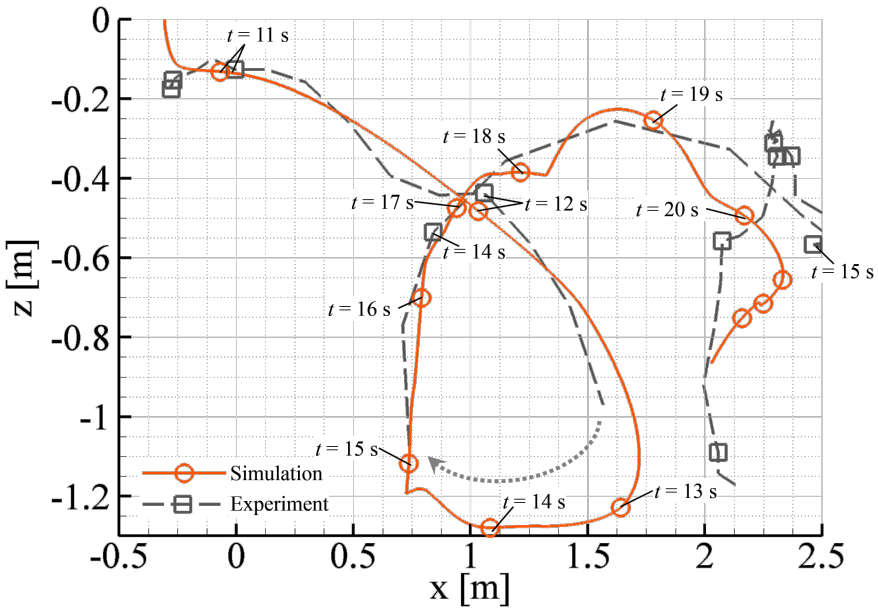

Fig. 11 An experimental and a simulated head tracking. The experimental result below z = -1.0 m is out of frame.

4. Application of simulation to lifejacket usage

4.1. Simulation conditions

The developed model was applied to simulations with lifejackets. For consistency with prior experimental work considered a manikin wearing a lifejacket of various buoyancy, lifejacket buoyancy of 3.5 kgf (34.3 N), 4.0 kgf (39.2 N), and 4.5 kgf (44.1 N) were applied to the trunk of the subject by adjusting its density in the simulation. The simulation was then performed under the computational conditions same as those outlined in section 3.2.

4.2. Simulation results

4.2.1. Movement of the human body The snapshots of the subject with 3.5 kgf, 4.0 kgf, and 4.5 kgf of lifejacket buoyancy after contact with the wave are shown in Fig 12. The flow vectors and non-static pressure distribution are shown on the cross section y = 0 m. Additionally, the vertical locations on the z-axis of the center of mass of the head and entire body are shown in Fig. 13.

Immediately after the subject left the blocks (t = 11–12 s), the upward flows of the wave in the area near the water surface rapidly raised the subject's upper body, while the subject's legs fell down from the blocks. As the wave passed the blocks (around $t \geq 11.5$ s), the subject passed over a circular area with a lower non-static pressure that occurred behind the blocks. At this point, variation in the vertical location of the center of mass was observed with each modeled lifejacket. Later ($t \geq 12$ s), with 3.5 kgf of lifejacket buoyancy (Fig. 12(a)), the subject was found to have completely submerged.

[DOI: 10.1299/jbse.18-00321]

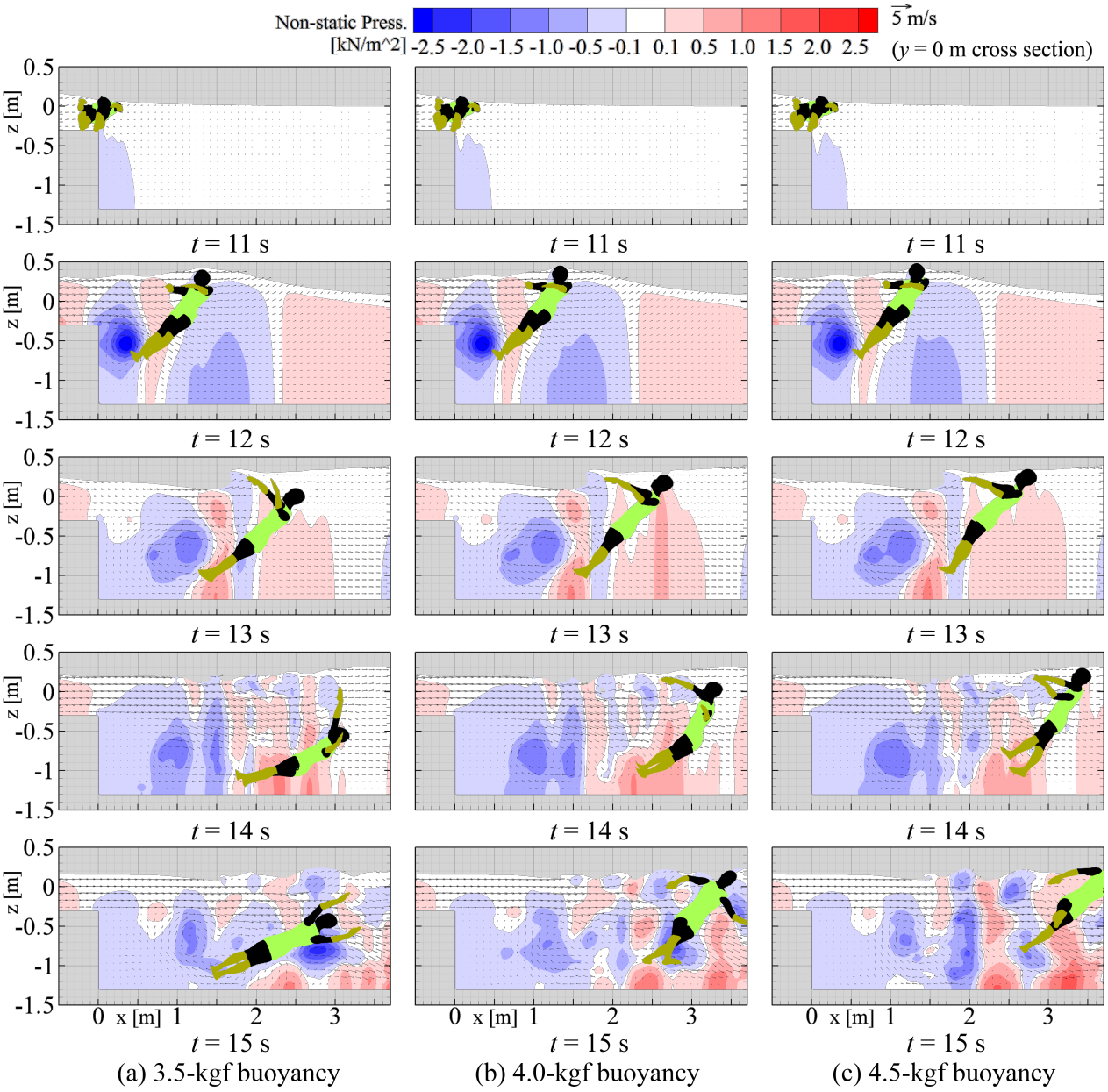

Fig. 12 Snapshots of the human body considered for simulation, with (a) 3.5 kfg, (b) 4.0 kfg, and (c) 4.5 kfg of buoyancy applied to the breast to simulate lifejacket usage.

With 4.0 kgf of lifejacket buoyancy (Fig. 12(b)), the subject was found to have slightly submerged until t = 14 s before its head rose again to the surface, and to continue drifting above water ($t \geq 15$ s). Finally, with 4.5 kgf of lifejacket buoyancy (Fig. 12(c)), the body drifted on the detached flow with its head afloat near the water surface.

Thus, the subject with a lifejacket buoyancy of 3.5 kgf did not float even the lifejacket buoyancy was greater than the weight of the subject (2.2 kgf). These results reveal that the forces from unsteady flows must be considered for the evaluation of lifejackets used in tsunamis, which is in contrast to the case of common lifejackets wherein strong flows are not considered (International Organization for Standardization, 2006a).

4.2.2. Receiving force In areas with higher vorticity (Fig. 8(a)), the non-static pressure was decreased by higher velocity (Fig. 12). Consequently, a force toward the center of the vortex was applied to the subject. These flows faced downward on the downstream side of the vortex and were applied continuously to the subject as the vortex spread. The forces causing the subject to sink are expected to be composed of such less pressure and downward flows. Thus, the amount of lifejacket buoyancy required to be afloat in tsunamis can be estimated by evaluating these forces in the comparison with location of the subject in the water currents. To confirm this expectation, next the vertical forces applied

[DOI: 10.1299/jbse.18-00321]

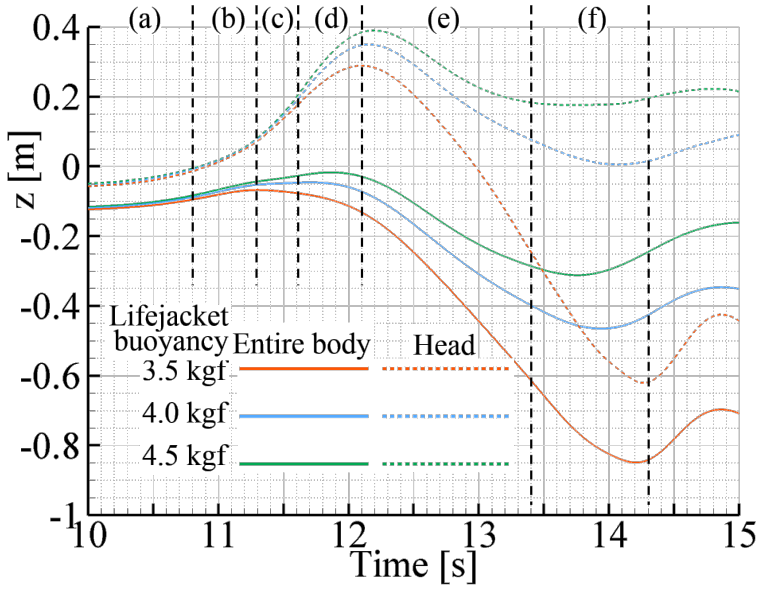

Fig. 13 Vertical location of the center of mass.

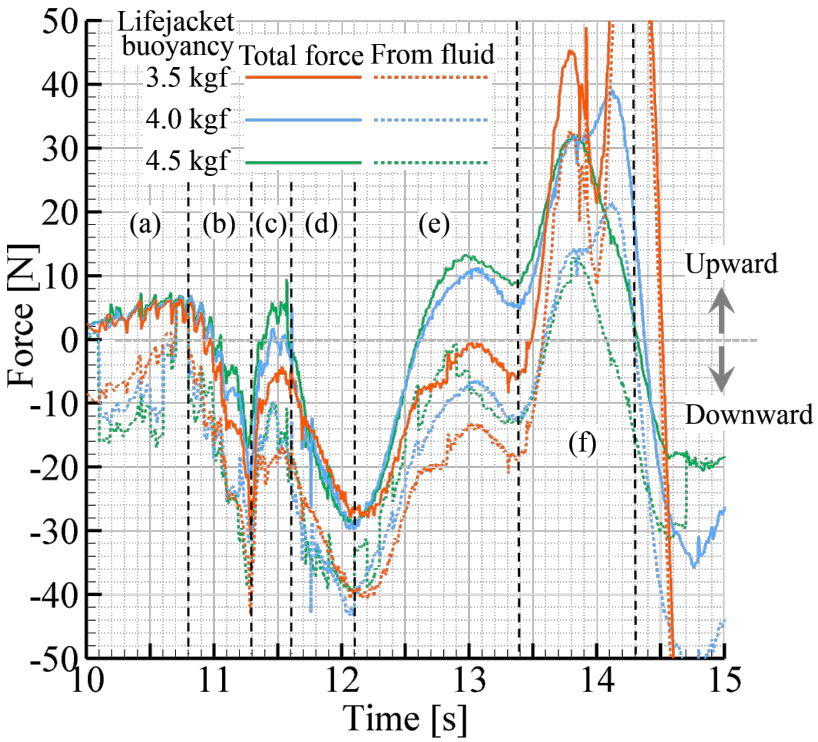

Fig. 14 Vertical force applied to the entire body.

to the entire subject are shown in Fig. 14, which showed a contrast with the movement in Figs. 12 and 13. In Fig. 14, in addition to the total force (solid lines), the force from the fluid flows was estimated (dashed lines) by subtracting the weight and buoyancy of the subject from the total force.

While the subject was on the blocks ($t \leq 10.8$ s: period (a) in Fig 14), the subject's upper body was kept afloat in all cases and received a slight upward force from rising water surface. In this period, the normal forces from the blocks prevented the subject sinking while the subject is receiving downward fluid force. Immediately after the subject left the blocks ($t = 10.8$–11.3 s: period (b) in Fig 14), downward forces were applied strongly from the fluid as the subject passed the vortex and the subject's legs were attracted by the low-pressure center. As the subject's upper body was raised by the

[DOI: 10.1299/jbse.18-00321]

wave (t = 11.3–11.6 s: period (c) in Fig 14), the downward force was temporally decreased. Although the amount of force from the fluid was similar in all cases, the lifejacket buoyancy varied the total force and consequently caused a divergence in the mass center. In t = 11.6–12.1 s (period (d) in Fig 14), the downward forces on the subject again increased as the subject's upper body reached the crest of the wave. Here, the total forces on the body were almost same in all cases, although they have different lifejacket buoyancy. This is because a part of the subject's head was not under water in the case of 4.0 kgf and 4.5 kgf of lifejacket buoyancy.

After the human body passed over the vortex (t = 12.1–13.4 s: period (e) in Fig 14), the downward force from the fluid was reduced because the subject had past above the vortex and thus attractive force to the center of the vortex was not applied vertically anymore. However, the legs (thighs, crura, and feet) remained near the vortex due to the attractive force and consequently were entrained by a downward flow until around t = 13.5 s. At t = 12 s, as shown in Fig. 12, the subject's feet were kept closer to the vortex with lesser lifejacket buoyancy, thereby receiving stronger downward force from the flows. With a lifejacket buoyancy of 3.5 kgf, the total force was always downward until t = 13.5 s, leading to the submergence of the entire subject. In contrast, with lifejacket buoyancies of 4.0 kgf and 4.5 kgf, the receiving total force switched from downward to upward at t = 12.6 s, allowing the subject to float back to the water surface. Next, strong upward forces were temporally (t = 13.4–14.3 s: period (f) in Fig 14) applied from the fluid in all cases because the subject's lighter arms remained near the water surface and received upward flows in the wave, although it was insufficient in the case of a lifejacket with a buoyancy of 3.5 kgf to adequately lift the subject to the water surface.

Overall, a human body with insufficient lifejacket buoyancy may be submerged and not be able to float again because of the following factors of downward force generated due to water currents: (i) the attractive force at the center of a vortex applied while the body is passing over it (t = 11.3–11.6 s: period (c) in Fig 14) and (ii) the force from downward currents on the subject's legs in the downstream side of the vortex (t = 12.1–13.4 s: period (e) in Fig 14). When a more attractive force from the vortex is received, stronger downward currents are received because the legs are kept closer to the vortex. The attractive and downward forces generated by the vortexes have not previously been considered in the evaluation of lifejackets. This is partly because it is difficult to recognize and evaluate the distribution of pressure and vorticity without simulations. However, the developed model has indicated that these forces are indispensable for the quantitative evaluation of lifejackets in order to prevent tsunami-related deaths.

5. Conclusion

In this paper, a numerical model to evaluate the movement of a human body and the performance of lifejackets in tsunamis was developed based on a combination of the CIP-CUP scheme and the link segment model. By reproducing experiments conducted in Kurisu et al. (2018), the developed model represented the unsteady movement of a human body in unsteady water currents with sufficient precision, confirming its suitability for tsunamis. As a result of a series of simulations with different lifejacket buoyancy, the lifejacket buoyancy required to be afloat is more than 4 kgf. However, needless to say, this threshold of buoyancy must not be adequate against all of tsunamis because the tsunamis have various conditions such as different wave heights. The most important findings in the present work are not the threshold value, but the following facts; the simulation indicated that the downward forces affected in tsunamis must be larger than that in still water due to the water currents, and the developed model successfully showed mechanisms that the water current in tsunami imposes downward forces on the subject through a decreasing pressure and entrainment by the vortex. In other words, these findings suggest us that the water currents should be considered to evaluate lifejacket effectiveness in tsunamis and we think the developed model can be helpful to the evaluation.

For continued evaluation of lifejackets with regard to their use in tsunamis, further studies are required in two main areas. First, the used human specifications should be expanded. For this study, anthropometric data were used and adjusted to match the weight and movable joint ranges of the manikin used in Kurisu et al. (2018). However, as shown in section 3.2, proper manikin movement was dependent on the adoption of different density for each human body segment. Thus, more accurate subject specifications are necessary. Second, future work should include the application of lifejacket evaluation with the developed model to the spatial scale of larger tsunamis. As discussed in section 3.3, the simulated water currents correspond to tsunamis that are in the tsunami advisory range of Japan Meteorological Agency (2013). However, much larger tsunamis, i.e., those more than 5 or 10 m in height, have struck in the past (Muhari et al., 2012) and are predicted to strike in the future (Cabinet Office, Government of Japan, 2012). Although the attractive and downward forces from vortexes are likely present in such cases, it is unclear whether these forces are dominant for the movement of a human body. Thus, simulations must be conducted for such cases and these forces should be examined. These future

[DOI: 10.1299/jbse.18-00321]

quantitative analyses by the developed model will be able to provide useful information for designing a lifejacket as an effective counter measure against tsunamis.

Acknowledgement

This work was supported by JSPS KAKENHI Grant Number JP16H03147.

References

Aoki, K. and Yamazaki, N., The role of joint resistance by passive tissues in human bipedal walking, The Biomechanisms, Vol. 14 (1998) , pp. 59–68 (in Japanese).

Cabinet Office, Government of Japan, On tsunami height, inundation area, and damage estimation caused by Nankai-trough huge earthquake, (2012) , URL: http://www.bousai.go.jp/jishin/nankai/taisaku_wg/pdf/shiryo.pdf, accessed on 2018/10/15 (in Japanese).

Fujii, N., Ae, M., and Miyashita, K., Simulation system of human movement based on link segment model and its application to sport movements, The Bulletin of Health and Sport Sciences: University of Tsukuba, Vol. 18 (1995) , pp. 117–126 (in Japanese).

International Organization for Standardization, Personal flotation devices — Part 2: Lifejackets, performance level 275 — Safety requirements, ISO12402-2 (2006a) .

International Organization for Standardization, Personal flotation devices — Part 9: Test methods, ISO12402-9 (2006b) .

Japan Meteorological Agency, Explanation about tsunami warning / advisory and tsunami information, (2013) , URL: http://www.data.jma.go.jp/svd/eqev/data/joho/tsunamiinfo.html, accessed on 2018/10/15 (in Japanese).

Japan Society of Mechanical Engineer, ed. Multibody dynamics (1) -Fundamental theory-, Colona Publishing Co., Ltd. (2006) (in Japanese).

Kajishima, T., Numerical simulation of turbulent flows, Yokendo Co. Ltd. rivesd edition (2014) (in Japanese).

Kim, J. and Moin, P., Application of a fractional-step method to incompressible Navier-Stokes equations, Journal of Computational Physics, Vol. 59 (1985) , No. 2, pp. 308–323.

Kouchi, M. and Mochimaru, M., AIST/HQL Human dimension database, National Institute of Advanced Industrial Science and Technology H18PRO-503 (2006) (in Japanese).

Kurisu, A., Suga, H., Prochazka, Z., Suzuki, K., Oguri, K., and Inoue, T., Potential technique for improving the survival of victims of tsunamis, PLoS one, Vol. 13 (2018) , No. 5, p. e0197498.

Mizuno, N. and Yamakawa, M., Numerical simulation of flow around human in underwater dolphin kick swimming, Transactions of the JSME, Vol. 83 (2017) , No. 845, pp. 16-00049 (in Japanese).

Muhari, A., Imamura, F., Suppasri, A., and Mas, E., Tsunami arrival time characteristics of the 2011 East Japan Tsunami obtained from eyewitness accounts, evidence and numerical simulation, Journal of Natural Disaster Science, Vol. 34 (2012) , No. 1, pp. 91–104.

Nakamura, R., Saito, H., and Nagasaki, H., Fundamental kinesiology, Ishiyaku Publishers, Inc. sixth edition (2016) (in Japanese).

Nakamura, T., Ajima, D., Aizawa, T., and Inoue, T., Development of a three-dimensional fluid-human coupled numerical simulation model toward a drowning prevention, Journal of Japan Society of Civil Engineers, Ser. B1 (Hydraulic Engineering), Vol. 73 (2017) , No. 4, pp. I_601–I_606 (in Japanese).

Nakashima, M., Satou, K., and Miura, Y., Development of swimming human simulation model considering rigid body dynamics and unsteady fluid force for whole body, Journal of Fluid Science and Technology, Vol. 2 (2007) , No. 1, pp. 56–67.

National Police Agency, The great east japan earthquake and the police, The Focus, Vol. 281 (2012) (in Japanese).

Xiao, F., A computational model for suspended large rigid bodies in 3D unsteady viscous flows, Journal of Computational Physics, Vol. 155 (1999) , No. 2, pp. 348–379.

Yabe, T. and Aoki, T., A universal solver for hyperbolic-equations by cubic-polynomial interpolation I. one-dimensional solver, Computer Physics Communications, Vol. 66 (1991) , No. 2-3, pp. 219–232.

Yabe, T. and Wang, P. Y., Unified numerical procedure for compressible and incompressible fluid, Journal of The Physical Society of Japan, Vol. 60 (1991) , pp. 2105–2108.

Yabe, T., Ishikawa, T., Wang, P. Y., Aoki, T., Kadota, Y., and Ikeda, F., A universal solver for hyperbolic equations by cubic-polynomial interpolation II. Two- and three-dimensional solvers, Computer Physics Communications, Vol. 66 (1991) , No. 2-3, pp. 233–242.

[DOI: 10.1299/jbse.18-00321]